Chapter 2

2. Observational Techniques

2.1 In Situ

There are two general categories of techniques that allow observations of the solar wind to be made; remote sensing observations from terrestrial or spacecraft mounted instruments and in situ sampling from spacecraft. Major characteristics of the solar wind that can be measured in situ, include the local magnetic field strength and orientation and solar wind particle velocity. It has to be emphasised that conclusions drawn from in-situ measurements are only applicable, with certainty, to local solar wind conditions.

In situ observations, while very accurate over local scales, are by their nature not easily accomplished. The instrument has to be space based with all the additional challenges associated with launching and maintaining a space mission. Despite this, numerous in situ solar wind experiments have been undertaken since the beginning of the space age, often in association with interplanetary missions (Mariner 2, for example).

Measurements made in situ characterise the behaviour of solar wind composition, particle energy and particle density of the sampled plasma. Plasma composition and temperature signatures from solar wind source regions are preserved in solar wind structure, throughout the traversal of the heliosphere. This means that observing such characteristics enables one to investigate the nature and potential location of the source region in the corona.

When plasma particles impact on a suitable material, a stochastic electrical discharge is produced which is directly measured by the instrument and can be output as data. This effect is exploited in mass spectrometers which use internal electric fields of different strengths to select particles of different charges and masses. Particles of different charges and energies will respond differently as they traverse the electric field and hence impact the detector at different positions thus enabling a differentiation to be made. Neutral particles will not respond to electric fields and hence can also be identified as they will impact the detector at different locations from particles of positive or negative charge.

In situ measurements of magnetic fields can also be made using magnetometers. The magnetometer exploits the effect of magnetic induction by immersing a conducting wire or antenna into a magnetic field and directly measuring the current generated as the motion of the spacecraft (and also the changing positions of magnetic field lines) alter the field strength and orientation around the antenna. Field strength can be inferred directly from the magnitude of the measured induced current.

In situ measurements provide direct measurements of solar wind parameters. As such, in situ observations provide a useful capability to characterise the "ground truth" of inferences made when combined with remote sensing observations (section 2.2) of solar wind features on a large scale.

2.2 Remote Sensing

The solar wind can be analysed remotely by observing electromagnetic radiation that it has emitted or interacted with in some form. A summary of the different solar wind properties that can be observed by the two different methods is shown in Table 2.1 and further details can be found later in this section.

Table 2.1 Comparison of measureable parameters using in situ & remote sensing.

Remote Sensing	**In-Situ**
Velocity	Velocity, Temperature
Density distribution	Magnetic field strength and orientation
Flow direction in plane of sky view	Composition
Morphological evolution	Temporal density variation

Table 2.1: Some basic solar wind parameters measureable by in-situ and remote sensing observations. The differences between the parameters measured by both categories is that remote sensing observations encompass global heliospheric properties whereas in situ measurements are localised – each category complements the other.

2.2.1 X-Rays

There have been a number of successful solar X-ray observation missions in recent years, including Yokhoh (example image in Figure 2.1), and Hinode. Early direct evidence of solar X-ray radiation was obtained from instrumentation mounted on sub-orbital rocket flights and these also provided the first real confirmation of the high temperature corona.

X-ray emission can also occur when solar wind streams interact with other objects in the heliosphere such as comets. Solar wind ions can undergo a charge exchange on encountering cometary gases and release X-rays in the process. This effect was first observed in 1996 (Lisse, 1996) using the ROSAT X-ray observatory.

X-rays can be directly observed using X-ray telescopes, which are themselves attached to a charged-coupled device. To focus the X-rays, a grazing-incidence mirror is used instead of a refraction lens or reflective mirror.

Figure 2.1: X-ray emission from features in the Solar Corona.

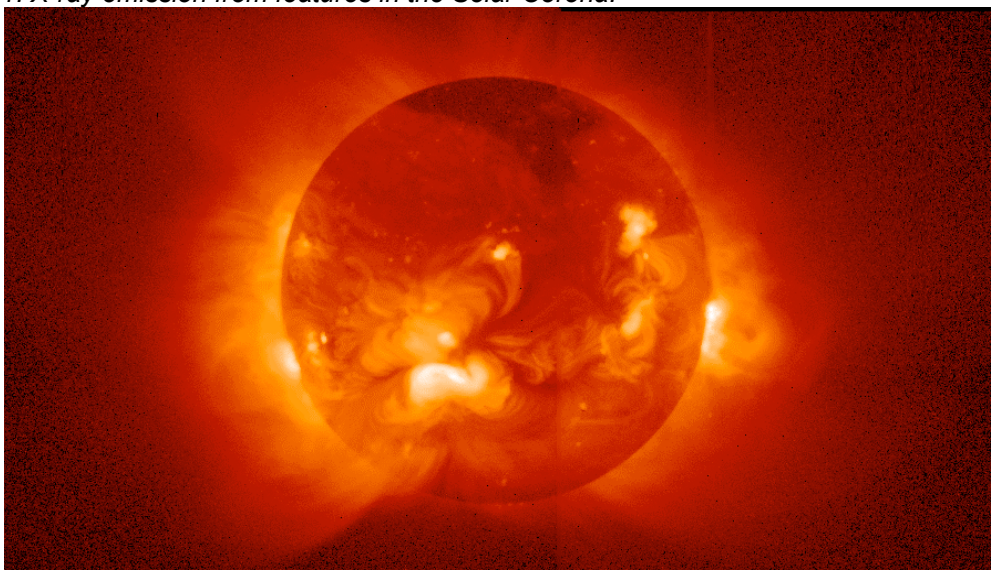

Figure 2.1: This is an example of X-ray emission from features such as coronal loops in the Solar Corona taken from the Solar X-ray Telescope on the Yohkoh spacecraft.(Image from University of Montana website).

2.2.2 Ultra-violet

As with X-rays, emission in ultra-violet light comes primarily from features in the hot corona. Ultra-violet and X-ray emission occur when a free electron in the corona passes close to a free ion. The electron is scattered by the free ion and releases a photon. The energy of the emitted photon is equivalent to the amount of kinetic energy lost by the electron during the interaction. This process is called Bremsstrahlung emission (Aschwanden, 2004).

Figure 2.2: X-ray and Extreme Ultra-Violet emission from the corona.

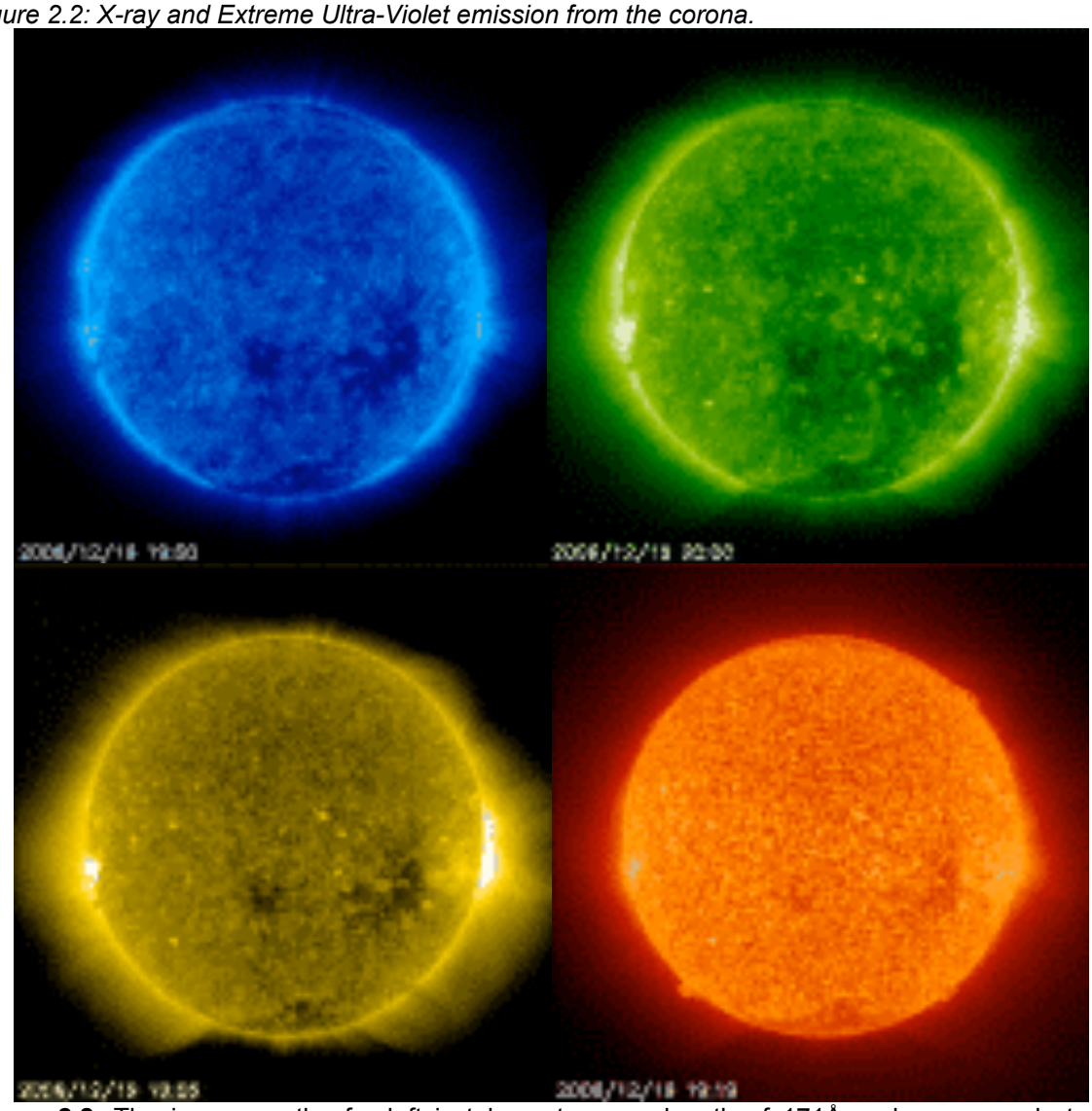

Figure 2.2: The image on the far left is taken at a wavelength of 171Å and corresponds to the components of the corona centred on temperatures of 10^6K. The green image is taken at a wavelength of 195Å and shows coronal material centred to temperatures of $1.5x10^6$K. The yellow image is taken at a wavelength of 284Å and corresponds to material at ~$2x10^6$K. The image on the far right corresponds to a wavelength of 304Å and material at ~$6x10^5$K. These images were taken on 15 December 2006 by the EIT on the SOHO spacecraft. (Images from European Space Agency Solar Heliospheric Observatory website).

Figure 2.2 is a montage of images taken by the extreme ultra-violet imaging telescope (EIT) onboard the SOHO spacecraft at different wavelengths. It should be noted that features observable at the different wavelengths are produced by material at a range of temperatures. For example, the image taken at 304Å contains light emitted from fully ionized Helium and partially ionized Iron, both at different temperatures. Bright areas of the images in Fig. 2.1 are active regions, usually

associated with sunspots. Darker areas (especially over the solar poles) are coronal holes. These are areas of significantly lower material density and are a source of fast solar wind streams (Krieger *et al*, 1973).

2.3 White Light

When a photon passes close to an electron it undergoes Thomson scattering (See Fig. 2.3). This occurs because the electric field component of the photon induces and acceleration in the electron. The photon is absorbed by the electron and re-transmitted due to the acceleration of the electron, maintaining the conservation of energy. As electrons are a major component of the corona and solar wind; observation of photospheric white light by Thomson scattering is readily available.

The received photons are collected by a charge-coupled device which records the impact of photons on individual pixels in the array as an electrical discharge. The number of discharges recorded from a given pixel in a given period of time enable a direct measurement of the received photon intensity to be made. Such devices are widely used in imaging instruments today, including those discussed in this thesis.

Figure 2.3: Thomson scattering.

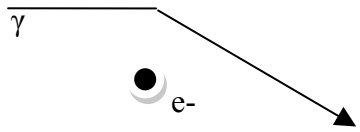

Figure 2.3: As the photon approaches a free electron it undergoes Thomson scattering, which alters the photon's trajectory. The K corona has a large electron component (Adapted from Aschwanden, 2004).

The equation of emissivity as a result of Thomson scattering in an area of a given electron density is given by equation 2.1.

$$i = I\ \sigma_{Th}\ N_{e-} \qquad \text{Eq. 2.1}$$

Where :

i = Scattered emission

I = Electron incident intensity

N_{e-} = Local electron density

σ_{Th} = Thomson scattering cross section ($8.85 \times 10^{-29} m^2$)

If it is assumed that the source of emission (the Sun) is isotropic then the electron incident intensity will be inversely proportional to the square of the distance between the emitter and the electron. If I_0 is the initial emission intensity at $1R_S$ and r is the distance between the Sun and the scattering region, equation 2.1 then becomes

$$i = \frac{I_0 \sigma_{Th} N_{e-}}{4\pi r^2} \qquad \text{Eq. 2.2}$$

The amount of Thomson scattered light that actually reaches the observer is comprised of a path integral of all scattering events along that line of sight. The sensitivity to scattering regions at certain distances along the line of sight is governed by the polarised nature of Thomson scattering emission from the corona.

The point where the line of sight passes closest to the Sun is the P-point (also see Section 2.4.2 on Interplanetary Scintillation). Consider a scattering region at a certain distance y along the line of sight from P, and at a distance r from the Sun as shown in Figure 2.4. The vibrations of free electrons in the corona induced by the incident radiation are distributed in a vibrational ellipsoid with the axes A, B and C (adapted from van de Hulst, 1950).

The intensity of the scattered emission (i from Eq. 2.2), that reaches the observer as a function of the axis J_t and J_r (where J_t is the tangential component and J_r is radial) will depend on the angle θ. The amount of scattered emission received by the observer from the AB plane (J_r) will be at a maximum when θ is 90°, or where y = 0.

Figure 2.4. Received scattering sensitivity to polarisation.

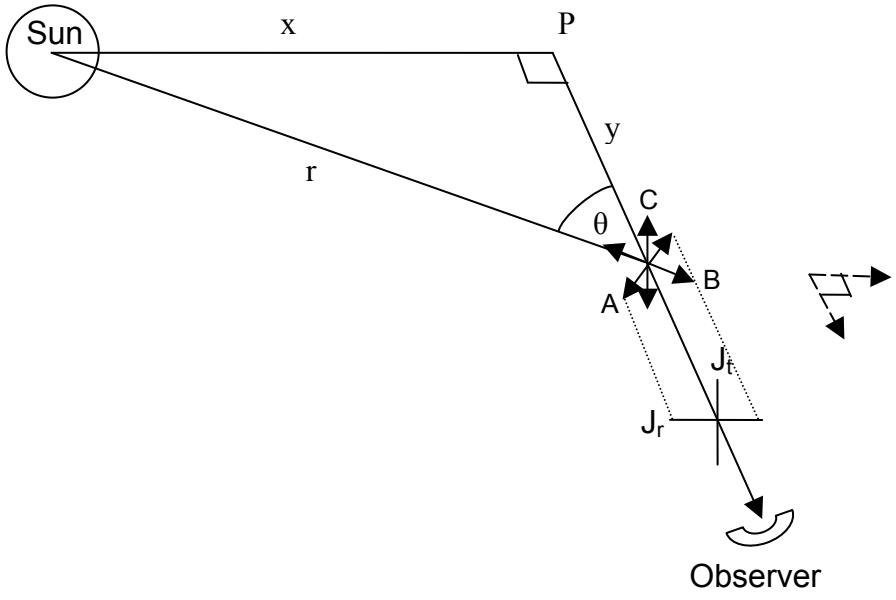

Figure 2.4 shows how the sensitivity to Thomson scattering from a scattering region along the line of sight is dependant on the distance of the region from the P-point. Maximum sensitivity to scattering occurs when θ=90° (Image adapted from van de Hulst, 1950).

If one were to connect all points in 3-dimensions at which θ = 90° then a spherical surface of maximum scattering sensitivity would be defined called the Thomson Sphere (Vourlidas and Howard, 2006), as shown in Fig. 2.5.

In a uniform solar wind; the location from which the most intense radiation is observed will emanate from the observers P-point along all possible lines of sight. In a non-uniform solar wind the most intense scattering may take place at some point along the line of sight other than at the P-point. This effect needs to be accounted for when making white light observations of phenomena such as CMEs for example, and this is examined in Chapter 4.

White light imaging favours observation of scattering events that are closer the observer over those that are further away. Since the intensity received at the observer is a function of a solid angle

Figure 2.5: The Thomson Scattering Sphere

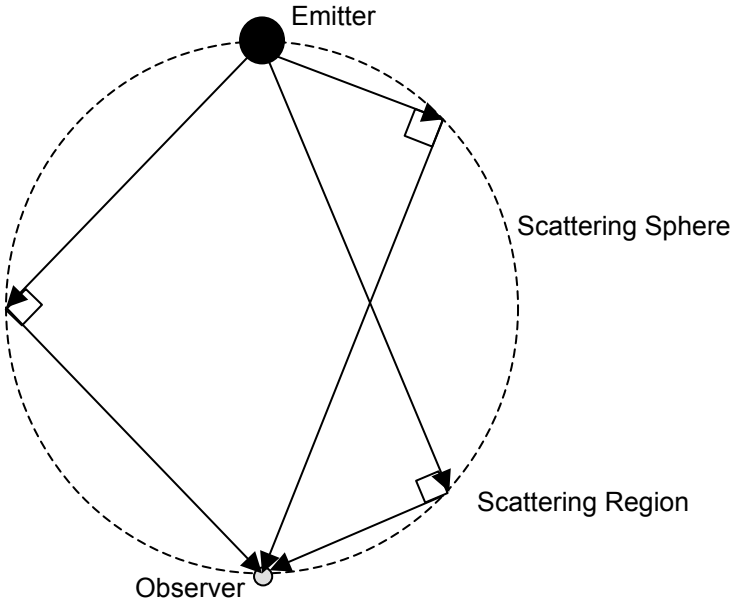

Figure 2.5: The most efficiently received radiation scattered in a uniform solar wind will emanate from the scattering regions along given lines of sight as shown. Each scattering region at the P-point for that line of sight makes up the Thomson sphere for a given observer. In a non-uniform solar wind, while the most efficient scattering may still take place at the P-point, the largest contributions to received intensity are likely to come from other locations along the line of sight. This situation is similar to the geometrical effects of the production of phase scintillations in the wave front from distant radio sources during IPS observations (see section 2.4.2 for more details).

White light observations are the oldest method of observing the corona as they are easily made with the naked eye during periods of total solar eclipse. The naked eye visibility of the corona is enhanced during these conditions as the lunar disk blocks the primary white light source (the photosphere) from view. This reduces the background level of white light, as seen by the observer, to below that of the intensity of the white light scattered from the corona.

The French astronomer Lyot was the first person to successfully artificially reproduce this effect, in 1930, by placing an occulting disk equal to the apparent diameter of the visible solar disk (photosphere) in the path of the light rays entering a telescope. This enabled the corona to be observed at times other than that dictated by the natural movements of the Sun and Moon, creating the first coronagraph (Fisher, 1995).

Earth based coronal observatories (with coronagraphs) still receive scattered Sunlight from our atmosphere. The crucial difference, for observation purposes, is

that atmospherically scattered light is relatively un-polarized in comparison with Thomson scattered light from electrons in the corona and solar wind. Therefore a ground based coronal observation can still be made by removing the un-polarized background light component from the image.

Background photospheric light that has been scattered off dust particles in the F corona (See Chapter 1) cause further problems for white light coronagraphic imaging. The intensity of the scattered light from both the F and K corona decreases with increasing distance from the Sun. From the photosphere to ~2.5R_S the light from the K corona outshines the F corona. However its intensity decreases more rapidly and beyond 2.5 R_S the light from the F corona becomes increasingly dominant. Figure 2.6 shows the comparative brightness of the two coronae.

Figure 2.6: Coronal brightness and electron density

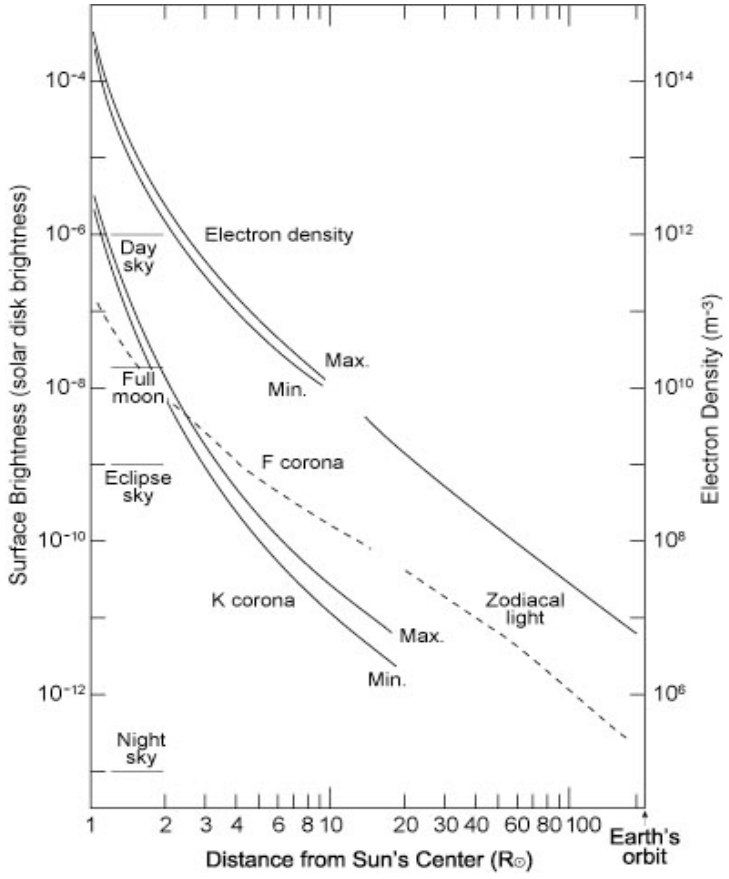

Figure 2.6: Coronal brightness contributions are shown from the different components as well as comparative brightness contributions from other heliospherical sources (Image from Howard et al., 2000).

In coronagraphic images the zodiacal light from the F corona must be subtracted from the image (See Fig. 2.6 for comparative brightness levels). The light from the K corona (which is the subject of white light images) is polarized, whereas the light from the F corona is not. This provides a method of distinguishing between the two and many white light telescopes imagers use some kind of polarization filter. A complimentary method is to use background subtraction, which is discussed in Chapter 3 in reference to white light data.

Over time, space based imagers can also start to become degraded due to the effects of radiation. Individual pixels in the imaging device (charged coupled device) can be permanently damaged by impacts from cosmic rays or radiation. The effects of these interactions are to create 'hot pixels' where a damaged pixel will constantly appear white in an image. Over time the numbers of these increase and must be taken account of during image processing.

2.3.1 Wide angle imaging

The occultation disk can be expanded in size to obscure not just the photosphere but the majority of the corona as well. If the imaging instrument behind the occulter is sensitive enough, it is possible to observe Thomson scattered radiation from the solar wind itself. More details of wide angle white light imaging data sources is given in Chapter 3.

The primary uses of wide angle observations are to examine the evolution of solar wind features as they traverse outward through the heliosphere. An example of a non-corongraph wide angle imager is the Solar Mass Ejection Imager, which is used primarily to track the progress of interplanetary transient features.

2.4 Radio

Observation of radio waves was one of the earliest methods of studying the Sun. The Earth's atmosphere is largely transparent to photons at these wavelengths and they can therefore be readily detected from ground based observatories. Indeed,

the first evidence of solar radio emission appeared soon after the development of radio communications. Solar radio noise caused numerous interference problems and engineers investigating these were the first to suggest a possible link. For example, Marconi declared in 1928 that radio signal strength seemed to vary in accordance with sunspot numbers. (Lanzerotti, 2004)

2.4.1 Radio Emission from the Solar Wind

Radio light can be emitted directly from particles in the corona and the solar wind during the passage of shock waves. These shock waves are caused by transient events such as solar flares. The shock waves travel outward from the initiation point (e.g. a solar flare) into interplanetary space.

As the shockwave passes through a given region of the solar wind it has the effect of temporarily increasing the local particle density. This has the knock on effect of increasing the local plasma frequency. Emission of radiation rises dramatically and occurs at a radio frequency that is dependant on plasma density. This increased emission is due to the presence of highly accelerated electrons in the shock region. A sufficiently high radio emission frequency brings the radio photons into the frequency domain detectable by ground based observatories.

2.4.2 Interplanetary Scintillation.

The solar wind is not an inherently featureless phenomenon, but contains a highly variable structure at many size scales. If a compact radio source, such as a quasar or pulsar, is observed from Earth when lying close to the Sun in the plane of the sky view then density fluctuations in the solar wind passing across the source beam induce phase variations across the wavefront. Radio signals from spacecraft can also be observed in this manner (e.g. Woo, 1978). The density fluctuations give rise to rapidly changing refractive indices of the solar wind medium and therefore alter the speed of light in the medium (e.g. Hewish et al., 1964, Rickett, 2006, Fallows et al., 2008).

The solar wind can be considered as a series of thin diffraction gratings orientated perpendicular to the source beam. The wave front of the source beam passes successively through each screen, simultaneously at many points. Due to the irregularities, each point of the source beam passage has a slightly different particle density. This causes light from different parts of the wave front to be scattered at different angles (Fig. 2.8) inducing phase variations across the wave front (e.g. Bourgois 1972, Saltpeter 1966).

With increasing distance from each thin grating the phase variations begin to constructively and destructively interfere with each other. Combined sections of the wave front that are in phase will produce maxima in the received signal profile. Sections that combine out of phase will destructively interfere with each other and produce minima on the received signal profile.

This process is analogous to starlight twinkling observed from inside our own atmosphere. The name derives from the fact that the source of the radio scintillation is located in the interplanetary regions of the heliosphere. A signal power profile received from the radio source by a suitable observatory on Earth would appear to fluctuate rapidly with time as density irregularities in the solar wind pass across the antennas line of sight (e.g. Hewish *et al,* 1964, Armstrong & Coles, 1972). These power fluctuations typically occur on timescales of 0.1 – 10s.

A distinction is made between “raypath” and “line of sight” in that in IPS the original photon emission source is a small diameter radio source, and the path these photons take through space is called the raypath. It is the passage of solar wind irregularities across this raypath that induces the phase scintillations in the wave front. In white light, however, the original emission source of the incoming photons is the Sun. The direction in which the observation in white light is orientated is called the line of sight. In both cases the most efficient scattering occurs at the P-point. However, again in both cases, a non-uniform solar wind will more than likely cause the most intense scattering along the line of sight (for white light) or the raypath (for IPS) to occur at some location other than the P-point.

Figure 2.7: Example of an IPS signal profile.

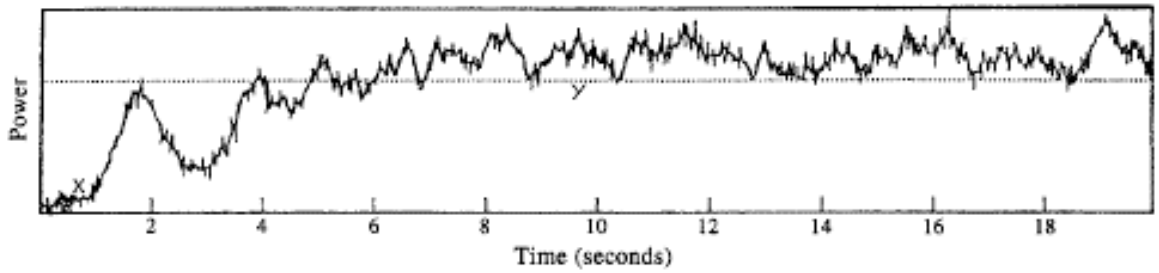

Figure 2.7: Power variation in the received radio source signal with time as observed in an IPS signal profile. The maxima and minima of the signal profile correspond to irregularities in the solar wind of differing particle density moving across the line of sight of the observing antenna. The point labelled X indicates a period in the observation where the antenna has not yet finished moving on to source. Position Y indicates when the antenna has arrive at an on source position. An increase in the received power can be clearly observed during this interval as the raypath from the source enters the field of view of the antenna (Image from Breen et al., 1996).

For scintillation to work in the way described here, the radio source must be approximately point like (Canals, 2002). In reality, many radio sources occupy some finite angular diameter in the sky and have inherent structure. Essentially this means that rather than having a single source beam, the observer effectively sees lots of separate source beams that are very close together, which originate from different parts of the source. Complications can arise if the angular diameter is sufficiently large that minima & maxima from the scattered beams overlap with each other. This creates extra scintillation in the received signal that is not as a result of interaction with the solar wind but self interaction with the individually scattered beams. Objects that are larger than point-like sources will have a smoothing effect on the amplitude variations, reducing the signal to noise ratio. If the source subtends an angle that is $\geq \frac{L}{D}$ where L is the average size of the solar wind irregularities and D is the distance from the irregularity to the observer the effect on the beam is a smoothing of the amplitude variations and hence a loss of IPS signal.

Figure 2.8: Solar Wind scattering modelled as a series of thin scattering screens.

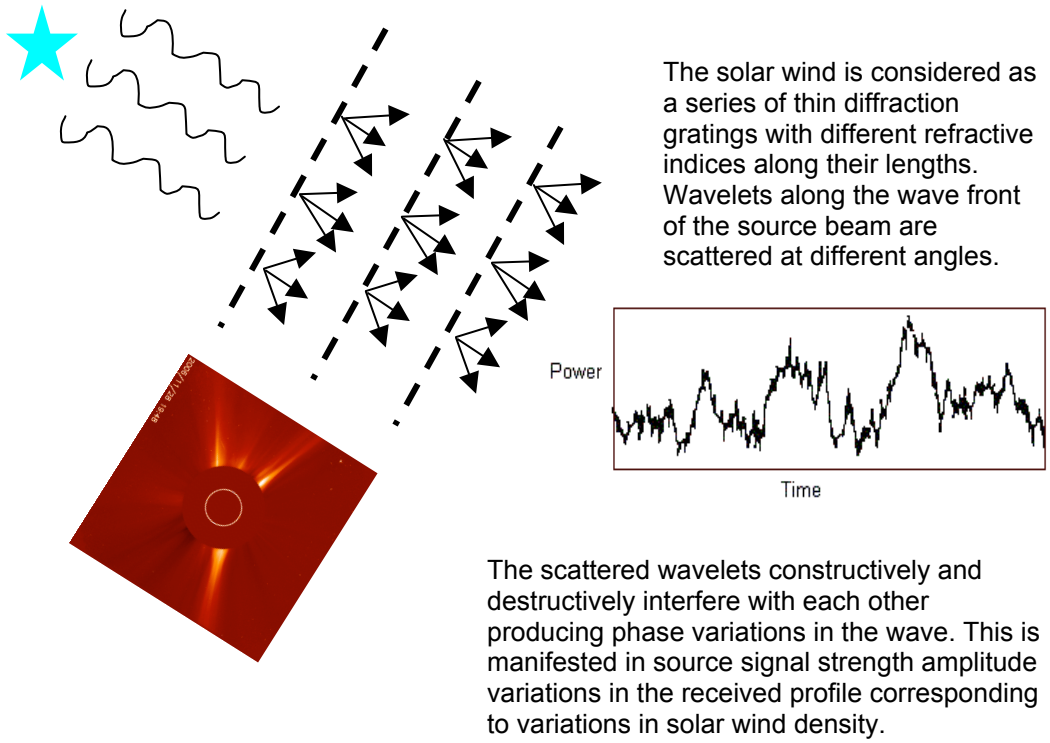

Figure 2.8: The series of scattering events in the thin screen approximation gradually 'wash out' the signature of the density variations in the signal profile. Higher frequency source photons are scattered less efficiently and can therefore preserve the density signatures over greater numbers of scattering events.

On passing through a scattering screen, the scattered source beam wavelets must traverse a sufficiently large distance that the interference patterns that give rise to scintillation are able to develop. This is called the Fresnel distance. If the distance between the scattering events and the observer are less than the Fresnel distance then the amount of scintillation observed will be reduced because the patterns have not had time to form before reception at Earth. The further away from the observer that scattering events occur, the greater the time available for the scintillation patterns to develop. This contrasts with white light imaging in which scattering events that take place at a greater distance from the observer are less detectable (see Section 2.3). A small majority of the observed scintillation is generated from scattering events on the source side of the p-point. This slight bias must be accounted for using a filter, called the Fresnel filter. This is covered more extensively in Fallows (2001) and Bisi (2006).

2.4.3 Measurements of scintillation level

Consider a plane wave from the radio source passing through a thin scattering screen, as described in Fig. 2.8. Phase variations will be induced across the wave front depending on the local refractive index on the screen. If x and y form the axis of the screen, as viewed from the perspective of the observer, then the refractive index at any point on the screem will be related to the electron density distribution across the screen in the x and y directions. The variation in local refractive index (n' in Eq. 2.3) and electron density are directly proportional to each other if the electron density variations are sufficiently small. Uscinski (1977) describes the refractive index as in Eq. 2.3:

$$n(x, y, z) = n_0 + n'(x, y, z) \qquad \text{Eq. 2.3}$$

Where:

n_0 = mean refractive index

$n'(x, y, z)$ = variation of refractive index about n_0

The variation in refractive index, n', is given as a function of x, y and z. The axis x and y are described above; z is the axis of the raypath and hence is perpendicular to the plane of the screen as defined by x and y. It is included in Eq. 2.3 for completeness (as in reality the scattering process is 3-dimensional). Because it is a thin scattering screen that is being considered, z is effectively negligible.

Refractive index variation is determined by the relative electric permittivity of the medium which, in the absence of particle collisions and a negligible influence from the magnetic field, can be represented as (adapted from Uscinki, 1977):

$$\varepsilon = n^2 = 1 - \frac{f_p^2}{f^2} \qquad \text{Eq. 2.4}$$

Where

$$f_p^2 = \frac{N_e e^2}{\varepsilon_0 m_e} \qquad \text{Eq. 2.5}$$

in which f_p is the plasma frequency, N_e is electron density (m^{-3}), e is the charge on the electron (1.6×10^{-19} C), ε_0 is the permittivity of free space (8.85×10^{-12} C^2 J^{-1} m^{-1}), m_e is the mass of the electron (9.11×10^{-31} kg) and f is the observation frequency. So, using Eq. 2.5, the plasma frequency for a volume of space with an electron density of 10^7 m^{-3}, is ≈ 178 kHz.

Because the plasma frequency (f_p) is much smaller than a typical observation frequency (e.g. 1.44 GHz, see Chapter 3), the refractive index can be expressed by

$$n = 1 - \frac{f_p^2}{2f^2} \qquad \text{Eq. 2.6}$$

Given that n' = n – n_0 (from Eq. 2.3), that the refractive index is directly proportional to electron density, and substituting for f_p, the variation of the refractive index about the mean can now be expressed by

$$n' = \left[1 - \frac{N_e e^2}{2f^2 \varepsilon_0 m_e}\right] - \left[1 - \frac{|N_e| e^2}{2f^2 \varepsilon_0 m_e}\right]$$
$$n' = \frac{\left[|N_e| - N_e\right] e^2}{2f^2 \varepsilon_0 m_e} \qquad \text{Eq. 2.7}$$

Where $|N_e|$ is the mean electron density across the screen and N_e is the electron density at a given position on the screen.

Therefore the refractive index of the solar wind is related to the particle density by simplifying equation 2.7 as shown below (adapted from Uscinski, 1977).

$$n' = \frac{\delta N_e e^2}{2f^2 \varepsilon_0 m_e} \qquad \text{Eq. 2.8}$$

The level of scintillation observed for a given radio source is more routinely defined by the *scintillation index* (Little & Hewish, 1966). The scintillation index is the

ratio of the rms variation in the received signal strength (at a given wavelength), due to scintillation, to the mean signal strength of the radio source. The mean signal strength of the source is that which is observed over the period of the observation.

$$m = \sqrt{\frac{\left(I - \bar{I}\right)^2}{\bar{I}^2}} \qquad \text{Eq. 2.9}$$

(Uscinki, 1977).

Where:

I = Signal strength of the incident radiation from the radio source at a given point in time

$\bar{I}$ = Mean source signal strength

Scintillation index is primarily dependent on observation frequency, source structure and the particle density of the solar wind crossing the raypath at the time of the observation.

Regions of the heliosphere that experience larger variations in electron density will scatter the incoming source beam more efficiently than regions of lower density variation. If the electron density variations of the regions are sufficiently large, then the average scattering angle of wavelets along the source beam wave front increases. This is problematic because with each successive scattering event along the ray path the signal profile of a specific density region will become increasingly indistinguishable from the signal profile sections of other density regions.

Hewish et al., (1964) noted that the scintillation level was related to the distance from the Sun at which the radio source was being observed in plane-of-sky distance. The scintillation levels are found to rise to a peak as the plane-of-sky distance between the Sun and the radio source increases. Beyond this peak the scintillation levels fall off. This peak occurs at the boundary between “weak” and “strong” scattering regimes. Under weak scattering conditions; the phase variations induced across the wavefront are typically much less than 1 radian. Under a strong

scattering regime the induced phase variations are considerably greater than 1 radian. Under strong scattering, the thin screen diffraction grating model cannot be applied, necessitating the use of full scattering theory. Thus IPS observations of a given frequency have an optimum plane-of-sky distance at which the scintillation index is highest. This effect is demonstrated clearly in Figs. 2.9 and 2.10.

As stated, the scintillation index is also dependant on observation frequency. This arises due to the different scattering angles that are induced by solar wind material on incoming photons of different frequencies (Coles, 1978). The solar wind in this sense acts in a similar way to visible light scattering in the Earth's atmosphere, in that photons of lower frequencies are less efficiently scattered than photons of higher frequencies. A plot showing scintillation index recorded for two radio sources observed at three different frequencies is presented in Figure 2.10.

Figure 2.9: Example of scintillation index variation with plane of sky distance

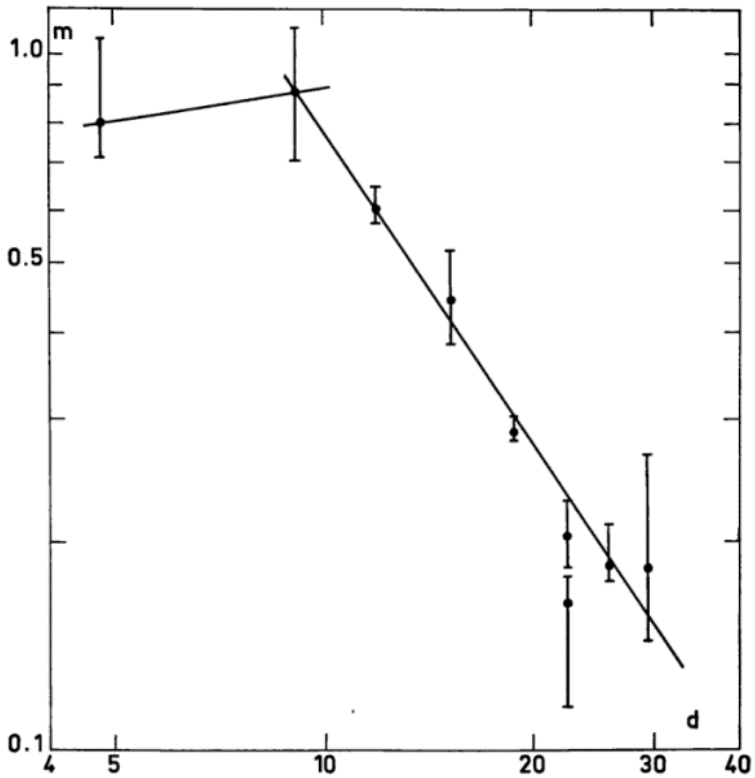

Figure 2.9: Scintillation index recorded for observations of radio source P 1148 – 00, plane of sky source distance in R_S (Bourgois, 1969). The peak of scintillation index occurs at approximately $10R_S$ and marks the boundary between "weak" and "strong" scattering regimes (Image from Coles, 1978).

Figure 2.10: Scintillation index variation with both frequency and plane of sky distance

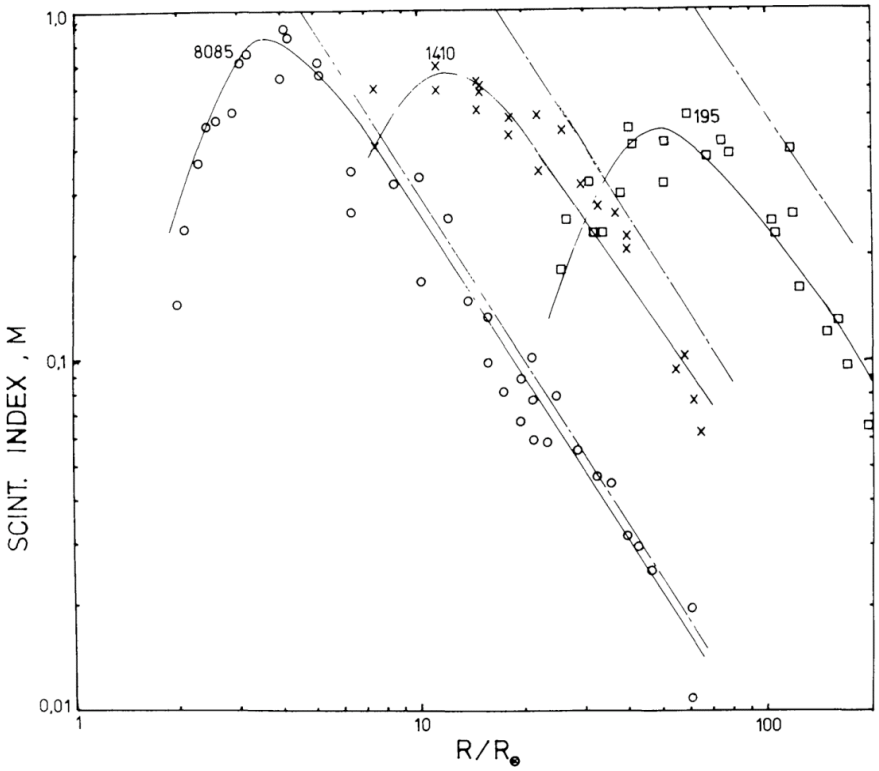

Figure 2.10: Scintillation index recorded for two radio sources. One source is 3C279 at 8.085 Ghz and 1.41 Ghz and the other is 3C138 at 0.195 Ghz. The peak in scintillation index lies further from the Sun in lower observing frequencies (Image from Coles, 1978).

2.4.4 IPS Observations.

The IPS observation of a given region of the heliosphere is possible only if there is a line of sight to a radio source that passes through that region. Secondly the radio source must emit at a frequency that will produce a good IPS signal after the beam has passed through the region on reception at Earth. Thirdly, because the geometry of the selected region of the heliosphere, the radio source location and that of Earth change throughout the year, observations must be made at certain times. If the radio observatories are ground based then they also have to be made during the times each day that the source is above the Earth's horizon at that geographic location.

Observations of the relatively high density regions of the solar wind near to the Sun therefore require higher frequency radio sources. Observations made further out require lower frequency sources (Fallows, 2001, Fallows *et al*, 2006). The

number of available radio sources decreases with increasing emission frequency and therefore it is more difficult to identify potential sources for observations close into the Sun. As lower frequency sources are considerably more numerous however it does mean that IPS observations can be made at all heliographic latitudes and at many solar radii. This makes IPS an extremely versatile observation tool which can probe many regions of the heliosphere that are inaccessible to in situ spacecraft sampling or unobservable in white light imaging.

If the radio source is observed simultaneously by two (or more) separate observation facilities then it is possible to calculate how fast a density variation in the solar wind is travelling (See Fig. 2.13).

Each receiving antenna will produce a signal profile such as that shown in Fig. 2.7. As the distance between the Earth based antennas and the radio source is so large the two lines of sight are effectively parallel. If a solar wind density irregularity flows outward through the heliosphere in a direction that will intersect the two lines of sight consecutively then the IPS signature of the feature will first be recorded at one antenna and then a short time later at the second. By observing the time delay between the signature appearance on the first antenna profile and its appearance on the second and combining this with knowledge of the distance, projected into the plane-of-sky, between the two lines of sight it is possible to calculate the velocity at which the density irregularity is traveling.

This technique is only sensitive to the radial component of solar wind velocity, and is therefore subjected to a cosθ effect when making velocity measurements of solar wind flow at all other angles. The signal profiles received at each antenna are a summation of all the scattering events along that antenna's raypath. However this technique is only sensitive to radial flow. At increasing distances from the P-point material crossing the line of sight does so at increasingly larger off radial angles.

Figure 2.11: Basic two point IPS observation.

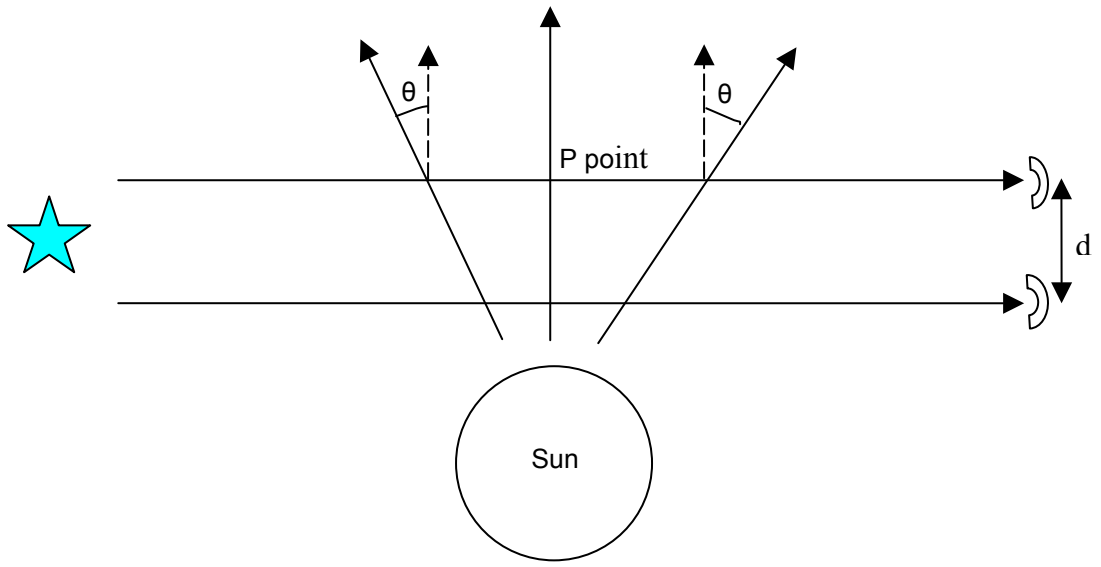

Figure 2.11: Two point IPS measurements are sensitive only to the radial component of solar wind velocity. The P point is the point of closest approach that the lines of sight come to the Sun and is therefore where the solar wind flow is completely radial from the perspective of the observers. The geographical distance (or "baseline") between the two antennae is denoted by d.

It is important to highlight the difference between scattering efficiency and scattering intensity. Scattering efficiency is the total amount of scattering events that take place in a given volume of space as a function of total particle density. As a first approximation, particle density decreases by $1/r^2$ where r is the distance from the scattering region to the Sun. The scattering potential of a given point along the raypath is also affected by a $1/r^2$ distance dependence, but in this case r is the distance from the scattering region to the P-point. Hence, to a first approximation, the relationship between scintillation potential and distance to the P-point decreases as $\sim \frac{1}{R^{-4}}$, where R is the distance along the raypath from the scattering region to the P-point. Scattering intensity refers to the intensity of the scattered light from the region in question that is incident on the imagers being used. Due to the distance to P-point relationship described for scattering potential; scattering intensity in IPS is therefore heavily weighted to regions of the raypath close to the P-point.

Figure 2.12: IPS radial flow sensitivity

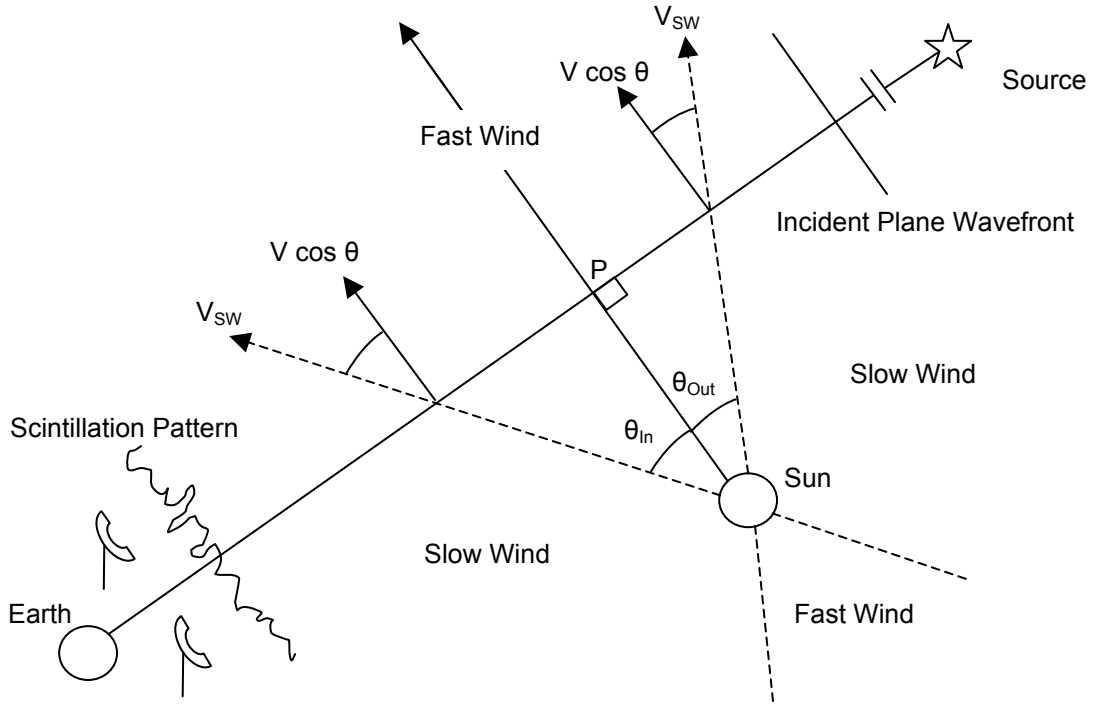

Figure 2.12 shows a two point IPS observation, with fast wind typically dominating over the polar regions and slow at more equatorial latitudes. The drifting scintillation pattern passes across the antenna on the right and then on the left. V_{SW} is the measured solar wind velocity. As can be seen, V_{SW}, is subject to cosθ effects. This method is only sensitive to the velocity component that is perpendicular to the line of sight. Scintillation is heavily weighted near to the P-point (Adapted from Massey, 1998).

2.4.5 The cross-correlation profile

Figure 2.13 shows an example of a cross-correlation analysis of the IPS signals received from two radio antennas during an observation. The dashed line and dotted lines (respectively) are the auto-correlation functions from the two antennas. The solid black line is the cross-correlation profile. A peak in cross-correlation of approximately 0.4, can be seen at a time lag of approximately 1.25 seconds. The projected plane-of-sky baseline is approximately 1000km, so if the plane-of-sky velocity can be determined simply by 1000 / 1.25 ≈ 800kms^{-1}, which is consistent with a fast stream solar wind flow.

Figure 2.13. An example cross-correlation profile.

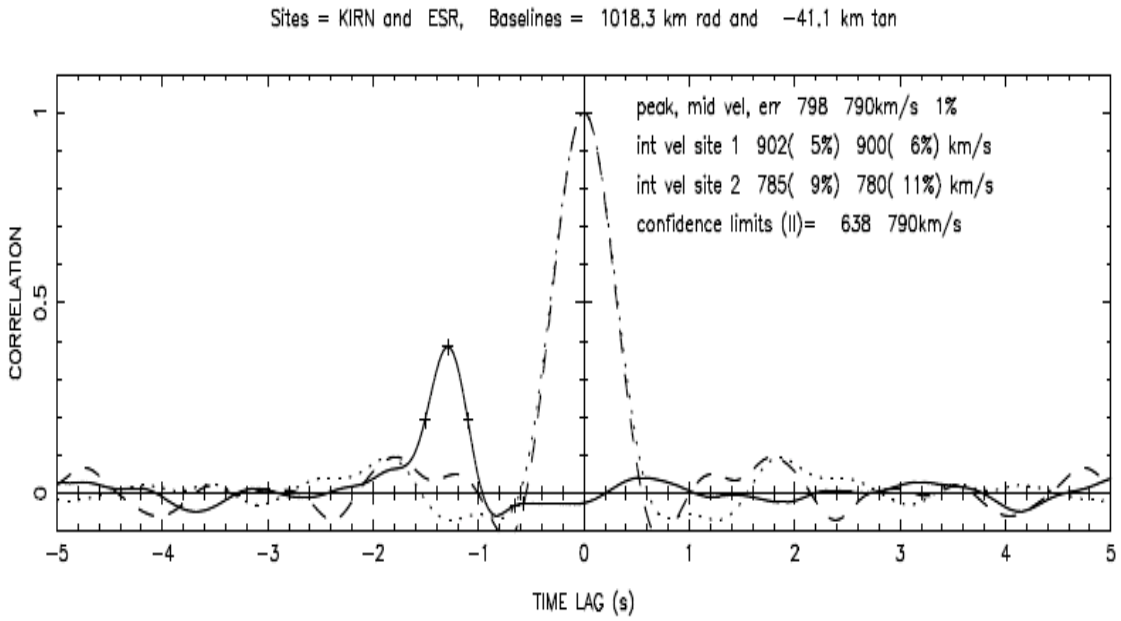

Figure 2.13 shows an example cross-correlation profile of a high speed solar wind stream, with a plane-of-sky velocity of approximately 800kms^{-1}.

During a dual antenna IPS observation, the rotation of the Earth has the effect of altering the orientation of the two receiving antennas with respect to the radial outflow axis of the solar wind. Observations are therefore deliberately timed to coincide with the time when the Earth's rotation carries the plane of the projected baseline through the radial axis of the solar wind flow. This is done because the degree of correlation between the signals received at each antenna will be at their highest at this point in time. Figure 2.13 shows an example of a single cross-correlation result comprising data from a fraction of an observation. As the plane-of-sky baseline rotates, it would be possible to observe the cross-correlation peak height rise and fall during a sequence of cross-correlation analyses from an observation period.

Similarly if there is any small angle off-radial deviation in the solar wind flow axis then again a suitably large baseline will give any features traveling along such a trajectory time enough to deviate significantly from the radial direction. On reaching the line of sight from antenna 2, the off-radial flow features will have deviated sufficiently that the maximum correlation occurring between the two signal profiles is

noticeable at a non-zero value for B_{perp} (See Figure 2.14, adapted from Moran et al., 1998).

Figure 2.14: Perpendicular and parallel baseline components.

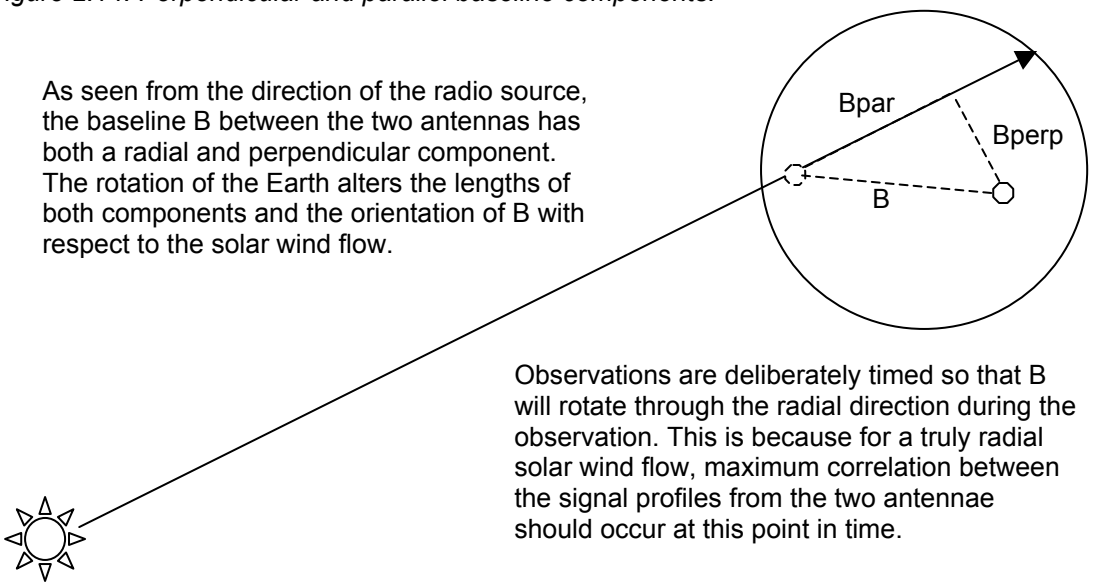

Figure 2.14: If solar wind flow is not strictly radial then maximum correlation between the two signal profiles will occur at some non-zero value of the perpendicular component of the baseline, Bperp. (Adapted from Canals, 2002)

If there are multiple solar wind streams within the line of sight, which are traveling at different velocities, a larger baseline will enable these streams to be more readily distinguished from each other. If two solar wind density features simultaneously move across the line of sight from antenna 1 at different velocities, then a sufficiently large baseline will give these two features time enough to separate from each other that they are individually resolvable by the time they cross the line of sight from antenna 2. This manifests itself in the cross-correlation profile as a broadening and lowering of the cross-correlation peak. If the baseline is long enough, it may even be possible to resolve two or more entirely independent solar wind streams. This would be represented by two or more cross-correlation peaks appearing at different time lags, corresponding to the different speeds of the streams (e.g. Breen et al., 1998).

Density irregularities in the solar wind are evolutionary phenomena. Over adequate time scales they will evolve. If the baseline between the two antennas is large enough then the solar wind features will decay significantly. This reduces the amount of correlation that can be obtained from the two signal profiles (Coles, 1978). This situation provides another avenue of research however in that it enables us to study the timescales involved in feature decay.

Cross-correlation analyses can also be used to detect the presence of solar wind transient features (CMEs for example) in the raypath. The magnetic field in a CME is rotated with respect to the general solar magnetic field configuration. The solar wind plasma is frozen into the magnetic field and will flow with these rotations as shown in Fig. 2.15. If the IPS raypath cuts through a region of rotated magnetic field then the scattering induced on the radio wave front will be affected by the presence of counter streaming electrons. This is manifested in the cross-correlation profile as a distinct lobe of anti-correlation occurring close to the 0 time lag (e.g. Canals, 2002). This is covered in more detail in Chapter 6.

Figure 2.15. Magnetic field rotation along the raypath.

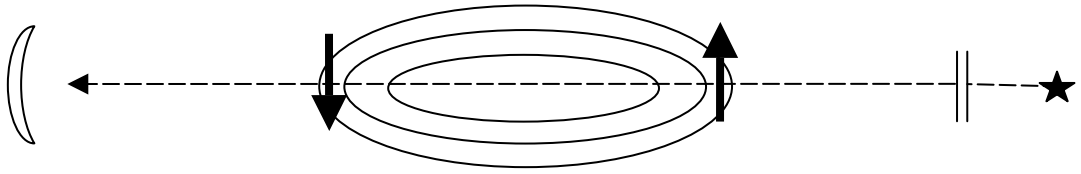

Figure 2.15 shows how the IPS raypath (dashed arrowed line) passes through a region of rotated magnetic field. Counter-streaming electrons (vertical thick arrows) contribute to the scattering, manifested in the cross-correlation profile by the presence of a lobe of anti-correlation near the 0 lag (e.g. Canals, 2002).

2.4.6 Dual Frequency Observations

Radio sources that are used for IPS observations emit radio waves at many wavelengths. This is advantageous because it increases the practicality of making observations with multiple telescopes. Telescopes at different facilities may not necessarily be capable of operating at different frequencies.

Fallows *et al* 2001 & 2006 have demonstrated successful dual point IPS observations for receiving antennas at significantly different receiving frequencies. These demonstrations included a simultaneous observation made by the 32m ESR radar antenna on the island Svalbard, receiving at 500 MHz and the EISCAT 32m antenna at Kiruna in Sweden, receiving at 1420 MHz.

This was possible because density irregularities in the solar wind that give rise to IPS at different frequencies overlap in terms of their physical size scales. Dual frequency observations have been used routinely for IPS observations by the Aberystwyth group since 2002 (Fallows et al., 2006. Fallows et al., 2008).